ARCHIVES OF MECHANICS
Arch. Mech. **78** (∗), ∗∗∗–∗∗∗, 2026, https://doi.org/10.24423/aom.4915

1D, 2D axisymmetric and 3D numerical simulation of valve-induced water-hammer

A. ALAVI*), K. URBANOWICZ

West Pomeranian University of Technology in Szczecin,
Faculty of Mechanical Engineering and Mechatronics,
Al. Piastów 19, 70-310 Szczecin, Poland
e-mail)*: *as61302@zut.edu.pl (corresponding author)*

In the present research, a numerical investigation of the classical water hammer problem induced by rapid valve closure in a reservoir–pipe–valve system is carried out. Multiple modeling approaches with different levels of spatial fidelity are developed, including a 1D Method of Characteristics (MoC) model with a convolution-based unsteady friction formulation, as well as 2D axisymmetric and 3D methods based on the Finite Volume Method (FVM). The full 3D solver is implemented in OpenFOAM open-source library and the Ansys Fluent commercial software, whereas the 2D axisymmetric is carried out solely in OpenFOAM. Since no 3D physics are explicitly applied to the solution domain, the 3D results remain basically 2D axisymmetric (no significant circumferential gradient is observed). The pressure responses obtained from the numerical models are compared with experimental results at the valve section. The improvement in prediction accuracy associated with increasing spatial fidelity is evaluated, and a detailed analysis of numerical dissipation and dispersion in all models is conducted. This study also investigates the effect of mesh resolution, particularly in the radial direction, time-step selection, and turbulence models on the prediction of pressure attenuation.

Key words: computational fluid dynamics, water hammer, unsteady friction, turbulence.

1. Introduction

Water hammer (WH) is a phenomenon that occurs in fluid transfer pipelines when the fluid is subjected to abrupt acceleration or deceleration. Such sudden changes in velocity could be a result of valve closure, load rejection in hydropower plants, pump shutdown or a number of other events causing transient behavior. Water hammer causes pressure waves forming in the pipeline, traveling back and forth in the fluid until they are completely damped due to friction. In most cases these pressure waves adversely affect the system, therefore they have been the subject of intensive research. Several approaches are available to study the formation of water hammer waves, including analytical, experimental and numerical methods.

Numerical approaches have attracted significant attention due to the advancement of open-source and commercial computational tools. Compared to experimental rigs, numerical models offer greater adaptability to different configurations and enable more detailed analysis through advanced post-processing tools. Numerical models also provide a strong basis for incorporating additional physics such as cavitation (column separation), fluid-structure interaction, gas pocket entrapment and other dynamic events including valve closure or load rejection in hydropower plants. The water hammer problem can be solved numerically at different levels of spatial fidelity: 1D, 2D and 3D. One-dimensional methods are beneficial for systems with long pipelines where gradients are primarily in the axial direction. In 2D simulations, radial variations are accounted for in addition to axial changes. Finally, 3D simulations resolve the full geometry of the fluid domain and are most useful for complex components such as pumps, reducers, valves, and any other hydraulic devices.

In hydraulic transient phenomena such as water hammer, modeling unsteady friction (UF) is essential. The way UF is incorporated differs across 1D, 2D and 3D numerical simulations. In 1D numerical methods, the system of partial differential equations governing the fluid motion is reduced to ordinary differential equations using the Method of Characteristics (MoC). In 1D models, UF is represented using several approaches, including convolution-based (CB), acceleration-based (AB) and quasi-steady (QS) models [1]. In terms of accuracy, CB formulations are generally the most reliable because they better reflect the underlying physical behavior of hydraulic transients. On the other hand, AB models account for UF through calibration and are therefore more prone to modeling error. Of all the UF modeling approaches, QS is the least accurate one since it assumes that the velocity profile is fully developed and calculates the friction factor from steady-state formulations such as Darcy–Weisbach and Colebrook–White formulas. These formulas are based on the cross-section-averaged velocity and do not take the deformation of the velocity profile into account.

One-dimensional modeling of water hammer is based on reduced continuity and momentum equations [2]. In these 1D equations, in order to compare the analyzed time histories of pressure and velocity changes with experimental results, it is necessary to calculate the wall shear stress using a formula that accounts for the effect of acceleration changes during the water hammer event. The most accurate approximation is provided by the convolution-based model originally developed by Zielke for laminar flow. In this work, in 1D model the wall shear stress is determined numerically using an efficient solution [3]. The applied approach eliminates the errors of the classical method identified by Vardy and Brown [4]. Laboratory water-hammer experiments in series-connected pipes of different diameters [5] were used to validate a 1D model based on the method-of-characteristics (MoC) with various quasi-steady and unsteady friction formulations. The study showed that accurate determination of pressure wave speed is crucial for matching measured and computed pressure amplitudes and frequencies, and two measurement-based methods for estimating wave speed were successfully evaluated. Using the proposed wave-speed determination and a numerical discretization that eliminates numerical diffusion enabled reliable verification of friction models without frequency discrepancies between experiments and simulations. Urbanowicz *et al.* [6] compared the results of 1D approach to quasi-two-dimensional (Q2D) model. Q2D models are somewhere between 1D and 2D models. These models consider the effect of radial changes of velocity on continuity and longitudinal momentum equation to directly calculate the wall shear stress from radial gradient of axial velocity. In Q2D, the momentum in the radial direction is not solved, therefore, it is called quasi-two-dimensional and not fully two-dimensional. Based on this study, both the 1D and Q2D models accurately reproduce water-hammer pressure responses in laminar flows, showing strong agreement with experimental data. For turbulent flows, Q2D model accuracy depends strongly on the Ghidaoui parameter, revealing limitations at low values and highlighting the need for further experiments. The Q2D model is computationally efficient even for long simulations and is thermodynamically consistent, whereas the 1D model violates the Clausius–Duhem inequality due to its inability to capture inner-layer energy dissipation. Martins *et al.* [7] found that closely timed operations in pipe networks can cause overlapping hydraulic transients that exceed design pressure limits. Through numerical and laboratory experiments on a reservoir-pipe-valve (RPV) system, the study analyzes how pressure waves generated by valve closure are damped over time using both detailed and simplified models. Based on this analysis, the authors provide practical guidelines to define a safe time interval between maneuvers to avoid hazardous pressure peaks. Just recently, Henclik [8] investigated water hammer events with column separation (CS) based on laboratory experiments in a copper pipeline equipped with elastic supports. Measurements of pressure oscillations and pipe vibrations showed that CS occurrence depends strongly on initial conditions and the stiffness of pipeline supports. The results demonstrate that more flexible pipeline fixing effectively reduces column separation intensity since more energy is absorbed by the structure through fluid-structure interaction.

Contrary to 1D methods, 2D and 3D numerical simulations are typically performed using the Finite Volume Method (FVM). In these approaches, unsteady friction is captured intrinsically, meaning that no additional UF model is required provided that the computational mesh has sufficient resolution. With the emergence of advanced Computational Fluid Dynamics (CFD) tools, researchers have attempted to develop axisymmetric 2D and full 3D simulations of the water-hammer phenomenon. Martins *et al.* [9] conducted a thorough mesh analysis for a CFD model of pressurized pipe flow. They introduced three mesh parameters: the axial sweep (streamwise discretization), the maximum mesh size in the circumferential direction, and the first-layer thickness in the radial direction. Using these parameters, they identified computationally efficient mesh resolutions for both laminar and turbulent flow regimes. Saemi *et al.* [10] investigated water-hammer effects in an RPV system under both laminar and turbulent regimes using 2D axisymmetric and full 3D CFD simulations. They optimized the three mesh metrics proposed in [9] and also examined the effect of time-step size on wave-attenuation results. The study suggests that asymmetric behavior can be observed within a distance of approximately one pipe diameter upstream of the valve. However, the 3D CFD model showed the best agreement with the experimental data. Martins and Wahba [11] developed Q2D, 2D axisymmetric, and full 3D simulations of water hammer for both laminar and turbulent cases and compared their solutions to experimental results. They showed that the Q2D and axisymmetric 2D models yield pressure responses that are almost identical to full 3D CFD, since the flow remains strongly one-dimensional in the studied configuration. Cao *et al.* [12] examined the effect of dynamic valve closure in 3D CFD simulations and compared the results with 1D MoC predictions and published experimental data. A dynamic-mesh approach was employed to model rapid ball-valve closure, which proved useful for visualizing the influence of valve motion on pressure-wave formation. Neyestanaki *et al.* [13] later conducted a comprehensive study of the valve-closure mechanism in a highly turbulent water-hammer case. They indicated that the sliding-mesh approach is the most efficient and accurate method for modeling the linear motion of a gate valve. Bergant *et al.* [14] studied water hammer via analytical and numerical approaches. They developed 1D and full 3D CFD simulations for laminar and low-Reynolds turbulent flows. The analytical solution and 1D MoC with frozen viscosity convolution formulation for UF modeling were accurate for low-Reynolds cases ($\mathrm{Re} < 10^4$), and the 3D CFD simulation also yielded low errors (2%–5%) for the same conditions. Martins *et al.* [15] examined the effect of blockages on valve-induced water hammer in a classical RPV system using three-dimensional CFD in OpenFOAM. Since such blockages introduce gradients in directions other than the axial one, CFD is well suited to capture the resulting flow non-uniformities and their influence on pressure-wave attenuation during valve closure. Vovk and Ravnik [16] compared a 1D MoC model based on the Euler equations with an added unsteady-friction formulation against a 3D CFD simulation in OpenFOAM for a pump-failure test case involving water hammer, cavitation, and column separation. In their study, one of the main advantages of the 3D approach is the ability to model cavitation and bubble formation directly within the flow field. Maskani *et al.* [17] developed a 3D CFD simulation and compared its results with 1D

MoC predictions using quasi-steady, Zielke, and Brunone formulations for unsteady friction. They employed an unstructured mesh, and the error in the 3D results increased as wave attenuation progressed over time, suggesting that the unstructured grid reduced accuracy.

Although numerous studies have investigated water hammer phenomena using either one-dimensional models or high-fidelity CFD simulations, the influence of spatial resolution and turbulence modeling on the accuracy of transient pressure prediction remains insufficiently understood. In particular, the role of near-wall resolution and radial mesh refinement in predicting pressure attenuation has received limited attention. In this study, one-dimensional Method of Characteristics (MoC), two-dimensional axisymmetric CFD, and full three-dimensional CFD simulations are employed and compared with experimental results available in the literature for a classical RPV system subjected to rapid valve closure. A detailed mesh sensitivity analysis is performed to determine the most efficient spatial resolution, while time-step sensitivity is also investigated. Simulations are carried out for both laminar and turbulent flow regimes. For the turbulent case, the standard k–ϵ and k–ω SST turbulence models are considered. Particular attention is given to the influence of radial mesh resolution and near-wall modeling on the prediction of pressure wave attenuation in CFD simulations of valve-induced water hammer.

2. Mathematical modeling and domain discretization

In this research, two test cases are selected for numerical replication. The first test case is adopted from HOLMBOE and ROULEAU [18] to investigate water-

TABLE 1. Technical information of test cases.

Parameter	Symbol and unit	HOLMBOE & ROULEAU [18]	SOARES *et al.* [19]
Pipe length	L [m]	36.088	15.22
Pipe radius	R [m]	0.01264	0.01
Pipe wall thickness	e [m]	0.00165	0.001
Acoustic wave speed	$c\ \left[\frac{m}{s}\right]$	1332	1255
Type of liquid	–	SAE–10 motor oil	Water
Dynamic viscosity	$\mu\ \left[\frac{\mathrm{kg}}{\mathrm{m\ s}}\right]$	0.0347	0.001
Density	$\rho_0\ \left[\frac{\mathrm{kg}}{\mathrm{m}^3}\right]$	875	998.2
Temperature	T [°C]	25	20
Reservoir pressure	P_R [Pa]	1.225×10^6	5.38×10^5
Reynolds number	Re [–]	81.5	8460
Initial steady-state velocity	$v_0\ \left[\frac{\mathrm{m}}{\mathrm{s}}\right]$	0.128	0.423

hammer waves in the laminar regime. The experimental setup consists of two reservoirs, a long copper pipe, and a ball valve equipped with a quick-closing apparatus to generate the water-hammer event. The second test case, chosen to study water hammer in the turbulent regime, is taken from Soares *et al.* [19]. This setup is also a classical RPV system in which water-hammer waves are generated by rapid closure of a ball valve in a copper pipeline. Table 1 summarizes the technical information for both test cases.

2.1. One-dimensional model

One-dimensional water hammer flow equations can be derived using at least three different approaches. In the first approach, the three-dimensional continuity and Navier–Stokes equations are simplified using the control-volume method, in which physical laws are applied to a finite fluid volume and subsequently a limit is taken as the volume becomes infinitesimal, without violating the continuum hypothesis [2]. The assumptions made to derive the water hammer equations in one dimension are:

- The flow is unidirectional, meaning the velocity vectors are parallel to the pipe axis.
- Pressure and density do not change in one cross-section of the pipe.
- There is no leakage in the pipe wall.
- The liquid is slightly compressible and the pipe wall is rigid.
- Low Mach number, meaning the convective velocity is much smaller than acoustic wave speed.

The above assumptions finally result in Eqs. (2.1) and (2.2) for momentum and mass conservation respectively. The reason why the advective term in the momentum equation is not present, is due to the low Mach number approximation. Writing the equations in non-dimensional form as in [2], causes the Mach number to appear in several terms of the system of partial differential equations. Since the flow is assumed to be low Mach number ($\mathrm{M} \ll 1$), these terms are crossed out and a much simpler system is to be solved for one-dimensional water hammer problem.

In the second approach, based on the integral formulation [20], the momentum equation is derived using the Reynolds transport theorem, whereby the fundamental laws are written for a flow within a specified region. In this derivation, flow variables are related to a control volume consisting of a specified mass of fluid fixed at a given pipe location. The boundary of the control volume is referred to as the control surface, while the exterior is the surroundings. In water-hammer analysis, the shape of the control volume varies in time due to changes in the internal pressure field. The continuity equation is derived by applying the law of mass conservation to the control volume and using Leibniz's rule, under the assumption of slight fluid compressibility and linearly elastic pipe walls, for which stress is proportional to strain.

In the third approach Wylie *et al.* [21] applied the principles of mass and momentum conservation to a free body of fluid with a cross-sectional area of a cylindrical or conical pipe. Analysis of the forces acting on a fluid slice, in comparison with inertial forces, leads to the equation of motion (for horizontal pipeline):

$$\rho\frac{\partial v}{\partial t}+\frac{\partial p}{\partial x}+\frac{2}{R}\tau_w=0, \tag{2.1}$$

where p – pressure at the pipe cross section, x – axial coordinate along the pipe, t – time, ρ – liquid density, v – mean velocity of the liquid at the pipe cross section, R – inner radius of the pipe, τ_w – wall shear stress. Furthermore, the analysis of a moving control volume, accounting for the conservation of mass, where the mass inflow into the control volume equals the time rate of increase of mass within the control volume, gives the continuity equation:

$$\frac{\partial p}{\partial t}+\rho c^2\frac{\partial v}{\partial x}=0, \tag{2.2}$$

where c is the acoustic wave speed (also known as the water hammer wave speed). The wall shear stress term appearing in the momentum equation (2.1) should be determined as summation of quasi-steady and unsteady component (Zielke convolution-based model):

$$\tau_w=\frac{\rho v|v|}{8}f+\frac{2\mu}{R}\int\limits_0^t\frac{\partial v}{\partial t}(u)\cdot w(t-u)\,du, \tag{2.3}$$

where f – Darcy–Weisbach friction factor, μ – dynamic viscosity of the liquid, $w(t-u)$ – time dependent weighting function (different in laminar and turbulent flow). This wall shear stress model can be computed efficiently using the numerical approach described in detail by Urbanowicz *et al.* [6], which eliminates the errors associated with the classical and computationally inefficient procedure originally proposed by Zielke [22]. Once the closing function required for the estimation of wall shear stress, Eq. (2.3), is specified, the resulting system of hyperbolic partial differential equations, Eqs. (2.1) and (2.2), is transformed into a system of ordinary differential equations using MoC and can be solved numerically. The numerical solution consists in transforming the original system into an equivalent set of four ordinary differential equations defined along the characteristic lines:

$$
C^{+} = \begin{cases} \dfrac{dx}{dt} = c, \\ \dfrac{1}{c\rho}\dfrac{dp}{dt} + \dfrac{dv}{dt} + \dfrac{2}{\rho R}\tau = 0, \end{cases}
\tag{2.4}
$$
$$
C^{-} = \begin{cases} \dfrac{dx}{dt} = -c, \\ -\dfrac{1}{c\rho}\dfrac{dp}{dt} + \dfrac{dv}{dt} + \dfrac{2}{\rho R}\tau = 0, \end{cases}
$$

which are subsequently solved using finite-difference approximations:

$$
\begin{cases} p_{t+\Delta t,i} \\ \quad = \dfrac{1}{2}[(p_{t,i-1} + p_{t,i+1}) + c\rho(v_{t,i-1} - v_{t,i+1}) + \dfrac{2c\Delta t}{R}(\tau_{t,i+1} - \tau_{t,i-1})], \\ v_{t+\Delta t,i} \\ \quad = \dfrac{1}{2}[(v_{t,i-1} + v_{t,i+1}) + \dfrac{1}{c\rho}(p_{t,i-1} - p_{t,i+1}) + \dfrac{2\Delta t}{\rho R}(\tau_{t,i-1} - \tau_{t,i+1})]. \end{cases}
\tag{2.5}
$$

The resulting system of algebraic equations enables time-marching determination of the primary flow variables, namely the velocity and pressure, at all internal nodes of the characteristic grid. In the simulations considered in this study, and subsequently compared with experimental data, the analyzed transient event is a water-hammer phenomenon caused by a rapid interruption of flow due to sudden valve closure. Accordingly, one boundary condition corresponds to a change in flow velocity from its initial steady-state value to zero.

In the present one-dimensional model, the valve section is assumed to be located at the first cross-section of the system, i.e. at the left end of the pipeline. At the opposite end of the pipe (right boundary), a constant pressure source is prescribed in the form of a reservoir with adjustable internal pressure, such that $p_{i=N+1} = \text{const}$, where N denotes the number of pipe reaches. This pressure remains constant both before and during the occurrence of the water-hammer event. The above boundary conditions lead to the following boundary equations within the MoC framework:

$$
\begin{cases} p_{t+\Delta t} = p_{t,2} - c\rho v_{t,2} + \dfrac{2c\Delta t}{R}\tau_{t,2}, \\ v_{t+\Delta t,N+1} = v_{t,N} - \dfrac{(p_{t+\Delta t,N+1} - p_{t,N})}{c\rho} - \dfrac{2\Delta t}{\rho R}\tau_{t,N}. \end{cases}
\tag{2.6}
$$

In all one-dimensional numerical simulations, the Courant–Friedrichs–Lewy condition (CFL) ($Co = 1$) was adopted. The spatial discretization of the pipeline also satisfied the Computational Compliance Criteria (CCC) [23], as the applied division $N = 32$ meets the requirement of this criterion, namely $N > 10$.

2.2. Two-dimensional axisymmetric and full three-dimensional CFD model

Governing equations for 2D axisymmetric and full 3D CFD models are the Reynolds-averaged Navier–Stokes equations in transient and compressible conditions, presented in tensor form [24]:

$$\frac{\partial \bar{\rho}}{\partial t} + \frac{\partial(\bar{\rho}\tilde{u}_i)}{\partial x_i} = 0, \tag{2.7}$$

$$\frac{\partial(\bar{\rho}\tilde{u}_i)}{\partial t} + \frac{\partial}{\partial x_j}(\bar{\rho}\tilde{u}_i\tilde{u}_j) = -\frac{\partial \bar{p}}{\partial x_i} + \frac{\partial \bar{\tau}_{ij}}{\partial x_j} - \frac{\partial}{\partial x_j}(\overline{\rho\, u_i'' u_j''}), \tag{2.8}$$

where $\bar{\rho}$ is the average density and $\tilde{u}_i$ is the Favre-averaged (density-weighted) velocity component defined as $\tilde{u}_i = \frac{\overline{\rho u_i}}{\bar{\rho}}$, $\overline{\rho\, u_i'' u_j''}$ is the Reynolds stress tensor, $\bar{p}$ is Reynolds-averaged pressure and $\bar{\tau}_{ij}$ is the mean viscous stress tensor denoted as:

$$\bar{\tau}_{ij} = \mu\left(\frac{\partial \tilde{u}_i}{\partial x_j} + \frac{\partial \tilde{u}_j}{\partial x_i} - \frac{2}{3}\delta_{ij}\frac{\partial \tilde{u}_k}{\partial x_k}\right). \tag{2.9}$$

2.2.1. Compressibility of liquid. To account for liquid compressibility, the density variation is related to the pressure variation through the bulk modulus. For a barotropic liquid, this relation can be written as [10]:

$$\frac{dp}{d\rho} = \frac{K_f}{\rho}, \tag{2.10}$$

where K_f is the bulk modulus of the liquid. If the effect of pipe-wall elasticity is also included without explicitly meshing the solid domain and solving a fluid–structure interaction problem, an effective (combined) bulk modulus can be used:

$$\frac{dp}{d\rho} = \frac{K_{f'}}{\rho}, \tag{2.11}$$

$$K_{f'} = \frac{K_f}{1 + \left(\frac{DK_f}{Ee}\right)}, \tag{2.12}$$

where D is the inner pipe diameter, E is Young's modulus of the pipe material, and e is the pipe-wall thickness. In the 3D CFD simulations, using the experimentally measured wave speed can improve the representation of compressibility:

$$c = \sqrt{\frac{K_{f'}}{\rho}}. \tag{2.13}$$

Finally, the barotropic equation of state relating pressure and density can be written in linearized form as

$$\rho = \rho_{ref} + \frac{p - p_{ref}}{c^2}, \tag{2.14}$$

where ρ_{ref} is the liquid density at a reference pressure p_{ref}, which is typically taken as atmospheric pressure. It is worth mentioning that since a pressure-based solver is used to solve the Navier–Stokes equation, density is expressed as a function of pressure.

2.2.2. Turbulence modeling. Two standard k–ϵ and k–ω SST models are used in this research which both use Boussinesq approximation [25] to obtain Reynolds stress tensor $\overline{\rho\, u_i'' u_j''}$:

$$\overline{\rho\, u_i'' u_j''} = -2\mu_t \tilde{S}_{ij} + \frac{2}{3}\bar{\rho} k \delta_{ij}, \tag{2.15}$$

where μ_t is the turbulent dynamic viscosity, k is turbulent kinetic energy and δ_{ij} is Kronecker delta. To close this equation, the turbulent kinetic energy and turbulent dynamic viscosity need to be calculated. The turbulent treatment approaches used in this study are explained comprehensively in [24], [25], [26] and [27].

2.3. Computational mesh

2.3.1. 3D mesh. The cylindrical domain is discretized in three directions and the mesh size is controlled using the parameters proposed by Martins *et al.* [9]. The mesh control metrics for the 3D CFD simulations are $\lambda_x = \frac{\Delta x}{D}$, $\lambda_\theta = \frac{\Delta r_\theta}{\pi D}$, $\lambda_r = \frac{FLT}{\delta}$ where Δx is the axial cell size, Δr_θ is the circumferential cell size (arc length), FLT is the first layer thickness in the radial direction and δ is the viscous sublayer thickness (commonly taken as $y^+ <= 5$). In the present work, δ is estimated from wall units as follows:

$$\delta = \frac{5\nu}{u_\tau}, \tag{2.16}$$

where ν is the kinematic viscosity and u_τ is the shear velocity defined as:

$$u_\tau = \sqrt{\frac{\tau_w}{\rho}}, \tag{2.17}$$

where the wall shear stress τ_w is calculated as below in steady flow:

$$\tau_w = \frac{f_D}{8}\rho v_0^2, \tag{2.18}$$

where f_D is the Darcy–Weisbach friction factor and v_0 is the averaged bulk velocity. The first and third metrics (λ_x and λ_r) are used for the 2D axisymmetric simulations, for which the circumferential metric λ_θ is not applicable. The mesh sizes used in the present study are summarized in Table 2 and representative laminar and turbulent meshes are shown in Fig. 1. A mesh sensitivity analysis is also carried out for both laminar and turbulence cases to determine the mesh size where solution is reasonably independent of it.

TABLE 2. Summary of the studied mesh metrics.

	Laminar			Turbulent		
λ_x	1.19	2.38	14.27	1.26	2.53	7.61
λ_θ	0.03571	0.05	0.083	0.0139	0.03125	0.05
λ_r	0.11	0.217	0.422	0.307	1.492	3.11

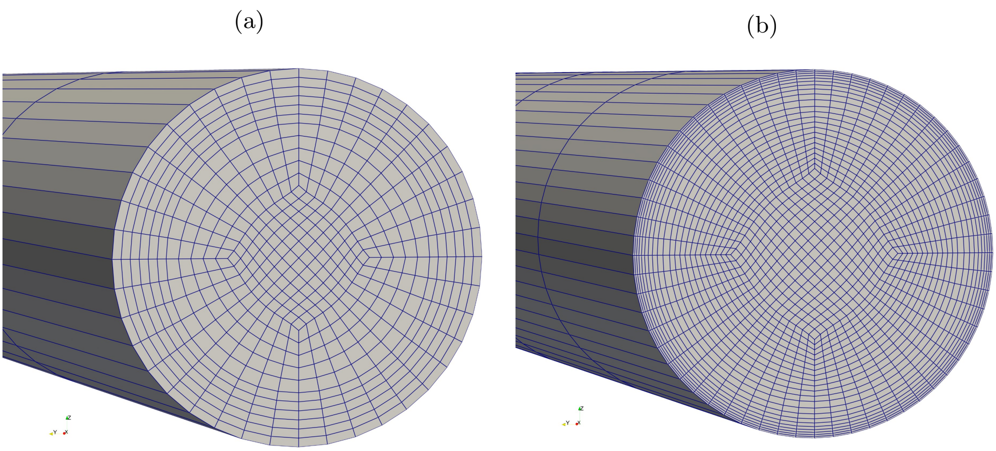

FIG. 1. An example of computational mesh for (a) laminar and (b) turbulent test cases.

The mesh sensitivity analysis is carried out based on mean absolute percentage error (MAPE) in this section. The formulation for MAPE is adopted from the works of [28–30]. This error parameter is defined to quantify the deviation of numerical and experimental results. MAPE is calculated from Eq. (2.19) to evaluate the pressure attenuation error at the valve boundary:

$$MAPE = \frac{1}{Z}\sum_{n=1}^{Z}\left|\frac{P^n_{sim} - P^n_{exp}}{P^n_{exp}}\right| \times 100\%. \tag{2.19}$$

In this equation, Z is the number of time-steps, subscripts *sim* and *exp* denote the simulation and experimental value, respectively, and superscript n is the index of time-step. The MAPE value indicates the average agreement between the pressure solution at the valve section and the experimental measurement.

The results of the mesh sensitivity analysis are presented in Figs. 2 and 3. As shown in Fig. 2, for the laminar case, mesh refinement in all three directions leads to stabilization of MAPE, indicating that the average solution has become independent of the mesh size.

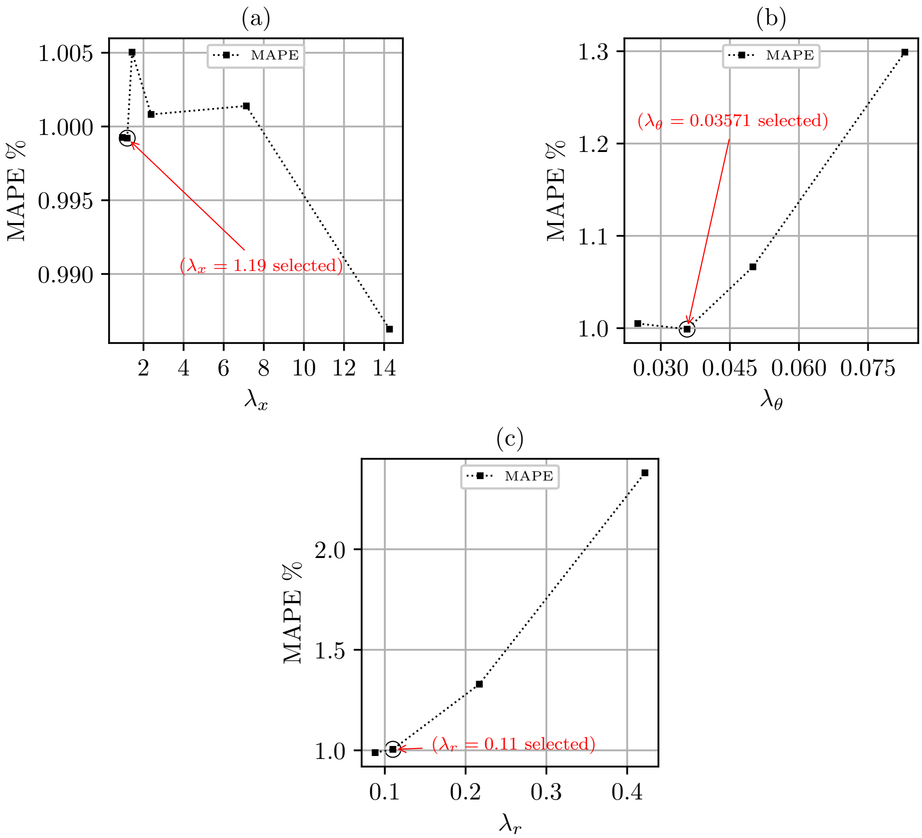

Fig. 2. Mesh sensitivity analysis for laminar test case in (a) axial, (b) circumferential, and (c) radial directions.

On the other hand, for the turbulent case, the variation in MAPE decreases to a sufficiently small value of approximately 0.25% for mesh refinement in the axial and circumferential directions (Figs. 3a and 3b). Beyond this level of refinement, further reduction in mesh size produces negligible changes in the results, which can therefore be interpreted as mesh-independent behavior. However, when refining mesh in the radial direction shown in Fig. 3c, the error does not converge. This behavior is attributed to the sensitivity of the turbulence

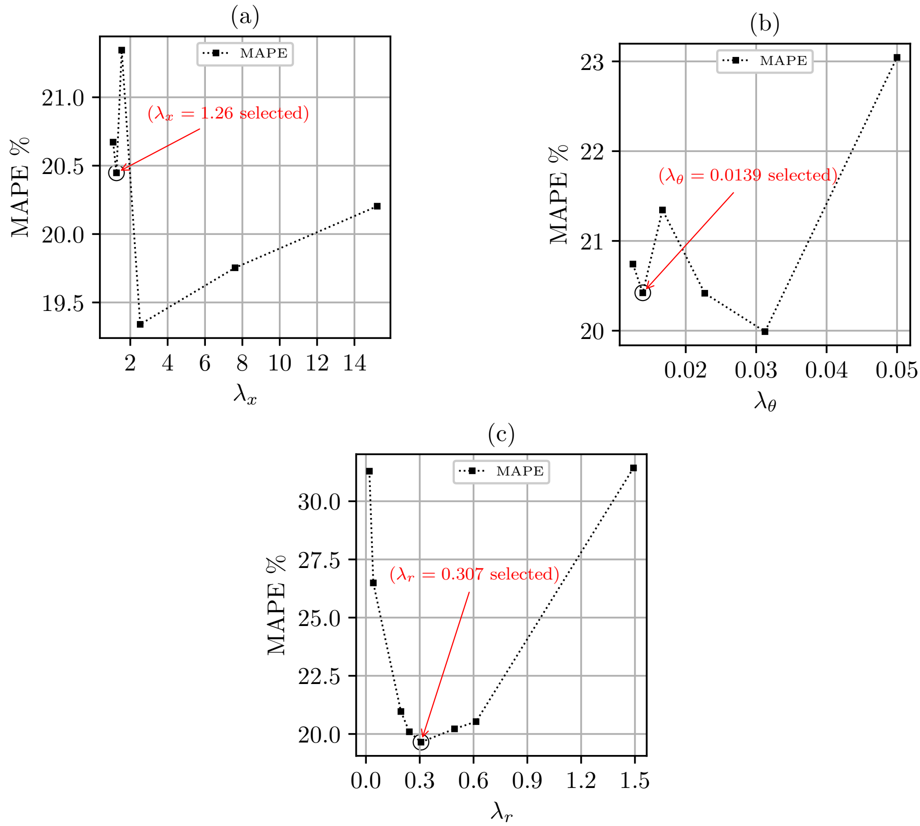

FIG. 3. Mesh sensitivity analysis for turbulent test case in (a) axial, (b) circumferential, and (c) radial directions.

model to the near-wall resolution. In transient pipe flows, accurate prediction of unsteady friction and energy dissipation strongly depends on the proper resolution of the viscous sublayer. SAEMI *et al.* [10] recommend maintaining y^+ values of approximately unity in order to obtain reliable results. In the present study, the minimum MAPE is obtained for $0.2 < \lambda_r < 0.4$, which corresponds to $y^+ \approx 1$. Further refinement of the near-wall mesh results in smaller y^+ values and leads to increased numerical damping of the pressure waves, indicating that excessive wall resolution may negatively affect the prediction of transient wave attenuation.

The mesh sensitivity analysis was conducted over the first water hammer period, corresponding to approximately one quarter of the total simulation time. The pressure peaks and wave attenuation within this interval are representative of the overall transient behavior. Extending the analysis to the full time span would significantly increase the computational cost without providing additional information regarding mesh convergence.

It is noteworthy that the larger values of λ_r for the turbulent case compared to the laminar one do not mean coarser mesh in the radial direction. This discrepancy is due to larger δ values for laminar flow regime, where viscous effects are dominant in the whole region, as opposed to turbulent flow where this is a narrow band close to the pipe wall. Therefore, λ_r values shall only be used when comparing cases with the same flow regime.

2.3.2. 2D axisymmetric mesh. The 2D axisymmetric solution is carried out in OpenFOAM. Figure 4 shows the computational domain for this model. In the 2D solution, only a small section of the full cylindrical pipe is selected. This geometry consists of 5 boundaries, 3 of them being identical to the 3D mesh (inlet, outlet and wall) with two additional boundaries acting as symmetry planes perpendicular to the circumferential direction in the pipe. All derivatives in the circumferential direction are neglected, although all 3 vector components still exist and vary in the axial and radial directions.

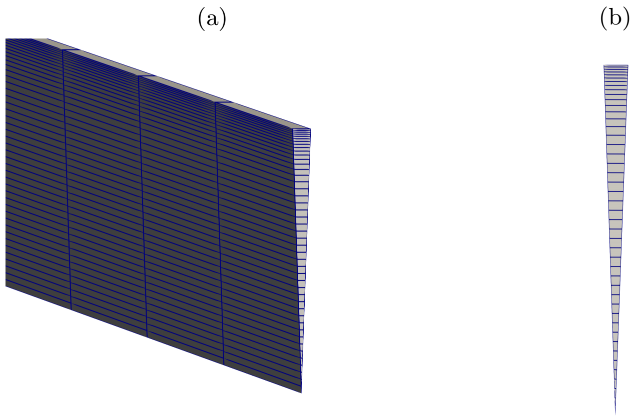

Fig. 4. Computational mesh for 2D turbulent case (a) isometric and (b) front view.

2.4. Boundary conditions

The present case consists of three boundaries, namely inlet, outlet, and wall. The computational tools ANSYS Fluent and OpenFOAM define and implement boundary conditions differently. Since boundary conditions in OpenFOAM can be stated more explicitly (and their description can be readily translated to ANSYS Fluent), this section focuses on explanation of the boundary conditions for OpenFOAM.

The simulations are carried out in two phases: steady and transient. The steady simulation corresponds to the valve-open configuration, where the fluid flows until a steady-state velocity and pressure distribution is obtained throughout the domain. After reaching the steady-state solution, the transient simulation begins by closing the valve. The valve-closure mechanism in this study is modeled by the abrupt change of velocity in the outlet from steady-state value to zero. For the steady simulation, the pressure is prescribed for both inlet and outlet as Dirichlet boundary condition equal to pressure at the reservoir for inlet and p_o for the outlet, calculated from Bernoulli's principle:

$$p_o = p_R - f\frac{L}{D}\rho\frac{v_0^2}{2}. \tag{2.20}$$

On the walls, the Neumann boundary condition is used which implies that the gradient of pressure in the direction normal to this boundary is equal to zero, meaning that no flow is crossing the walls. Since the pressure is prescribed for the inlet, velocity at this boundary is calculated based on the pressure gradient in the neighboring cell of the boundary, using the following equation:

$$\vec{U}_{boundary} = \vec{n}\frac{\phi}{\rho A}, \tag{2.21}$$

where $\vec{n}$ is the normal vector of the boundary, ϕ is the mass flux and A is the surface area. However, for the outlet, the velocity gradient normal to the boundary is set to zero, meaning that the fluid is freely flowing out of the domain. For the walls, the velocity is set to zero meaning that the no slip condition is used.

When moving on to the transient part of the simulation, the inlet boundary conditions are kept the same as the steady-state simulation. In the outlet, the sudden closure of the valve means zero velocity at this boundary, therefore, the pressure gradient normal to this boundary is also changed to zero to impose that no flow is crossing the valve. The boundary conditions used for the simulation are summarized in Table 3.

Table 3. Summary of boundary conditions.

	Steady		Transient	
Boundary	Velocity	Pressure	Velocity	Pressure
Inlet	pressureInletVelocity	$p_\Gamma = p_R$	pressureInletVelocity	$p_\Gamma = p_R$
Outlet	zeroGradient	$p_\Gamma = p_o$	$u_\Gamma = 0$	zeroGradient
Wall	$u_\Gamma = 0$	zeroGradient	$u_\Gamma = 0$	zeroGradient
Symmetry planes	wedge	wedge	wedge	wedge

For symmetry planes in the 2D axisymmetric simulation, the "wedge" boundary condition in OpenFOAM is used. This boundary condition sets derivatives in the direction perpendicular to the boundary to zero, which in this case is the circumferential component of the gradient vector.

2.5. Numerical procedure

In the present study, the OpenFOAM open-source library and Ansys Fluent commercial software are used to solve the water-hammer problem using FVM. For the steady solution, the Semi-Implicit Method for Pressure-Linked Equations (SIMPLE) algorithm is used. In this approach, there are several steps which finally lead to the solution of the Navier–Stokes equation. The steps are:

a) The velocity field is predicted using a guessed pressure field.
b) The coefficient matrix of the momentum conservation equation is updated with the current predicted velocity.
c) Using this coefficient matrix, the pressure equation is solved with the existing predicted velocity field.
d) Using the latest calculated pressure field, the velocity is explicitly updated.

At the end of this process there are a pressure field and a velocity field that neither satisfy the continuity and momentum conservation equations simultaneously. To reach a fully converged solution, the process starts over from step (a), and this time instead of a guessed pressure field, the one obtained in the last iteration is used. This cycle repeats until the difference between the newly calculated pressure and velocity and that of the previous iteration, falls below the convergence criterion prescribed by the user. This algorithm is widely used for steady state solutions. For transient solutions, the Pressure-Implicit with Splitting of Operators (PISO) algorithm is widely used. This algorithm is almost identical to the SIMPLE algorithm with loop repeating over steps (b), (c) and (d) (inner loop) instead of (a) to (d) (outer loop). This method is normally used when the solution is transient and the time-step is small enough to make a diagonally dominant coefficient matrix. This causes the pressure-velocity coupling loop to converge faster and makes this a convenient choice for transient problems where a large number of time-steps need to be solved. It is worth mentioning that in both methods, a non-orthogonality corrector also comes into play which loops over the solution of pressure equation to overcome non-orthogonality of the mesh cells. This can range from 0 for perfectly orthogonal computational cells to higher numbers for simulations where cells are non-orthogonal. Ferziger [31] explains the existing methods to solve the Navier–Stokes equation in detail.

To employ the advantages of SIMPLE method, namely its accurate results and PISO method for its faster convergence, the PIMPLE algorithm [32] is developed in OpenFOAM framework. This algorithm consists of both inner and outer loops for pressure velocity coupling in addition to non-orthogonality corrector to account for not perfectly orthogonal computational cells. This allows for choosing relatively larger time-steps and reaching the convergence criterion faster compared to PISO. On the other hand, PISO algorithm is widely used in Ansys Fluent for transient problems.

To reach a system of linear equations solvable by the above methods, the Navier–Stokes equation shall be discretized. A first-order implicit time scheme is used for temporal discretization in both software packages. This method is 1st order accurate in time and guarantees boundedness and stability.

The spatial schemes are used for discretizing convection, diffusion, gradient and source terms in the momentum transport equation. Using FVM requires the solver to calculate properties on cell faces despite the fact that they are known and stored in cell centers. As the derivation of the discretized transport equation is not within the scope of this work, only the used methods and their characteristics are mentioned.

For gradient terms, the cell-based Green–Gauss method is used in OpenFOAM which calculates the gradient using the face values. This approach gets more inaccurate as the mesh cells get more unstructured and skewness rises. Since the present mesh does not suffer from skewness and non-orthogonality, the present method suffices to get an accurate solution to the water hammer. On the other hand, in the case prepared in Ansys Fluent, the weighted cell-based least squares method is used, which is recommended by the software as a default setting for gradient calculation. In this method, the gradient in each cell center is calculated from solving an over-determined linear system of equations for each cell with the least squares method to minimize error of the solution. Conversely, this method relies on cell center values rather than cell faces and is less sensitive to increases in mesh skewness and non-orthogonality. Both methods are second order accurate in space, therefore, the two methods are expected to yield similar levels of accuracy when calculating gradients.

For discretizing the convection terms, there are a number of schemes available which are comprehensively described in Jasak PhD thesis [33]. The "Gauss limited linear" method used in OpenFOAM is a blend of upwind and linear methods to employ the stability of the upwind method without suffering from its diffusive characteristic. The Sweby [34] limiter is used in this case to bound the solution and prevent instability. The "Second order upwind" method used in Ansys has the same features as the "Gauss limited linear" method used in OpenFOAM, although it is inherently bounded and does not require the use of a limiter. They are both 2nd order accurate in space and bounded, so they don't cause non-physical oscillations and instability in the solution process.

For discretization of the diffusion term, the "Gauss linear corrected" and "Second order" methods are used in OpenFOAM and Ansys, respectively. Both methods are based on Gauss theorem, although named differently. The "Gauss linear corrected" term refers to using the Gauss theorem and assuming linear change of properties within one computational cell, which results in second order accuracy in space. The correction term indicates that OpenFOAM uses a non-orthogonality corrector for calculating the gradient on face center. This means that the orthogonal and non-orthogonal parts of the gradient are separated and the orthogonal part is treated implicitly while the non-orthogonal correction is treated explicitly. The same method in Ansys, is named "Second order" which identifies the order of accuracy in this method. Further information regarding non-orthogonal corrector is discussed in the literature [24, 33].

Throughout the discretization of the Navier–Stokes equation, there are some terms requiring values on cell faces rather than at cell centroids. One of the most important properties is the mass flux on faces of computational cells. For this purpose, the flux is calculated from the density and velocity values on the face. Therefore, an interpolation scheme shall be chosen to calculate the properties on faces from the cell center values. For both OpenFOAM and Ansys, the linear scheme is used for interpolation. This means that values vary linearly between two cell centers and the face value is calculated using a central difference.

The spatial discretization schemes are summarized in Table 4.

Table 4. Summary of spatial discretization schemes.

Terms	OpenFOAM	ANSYS Fluent
Gradient	Gauss linear	Least squares cell based
Convection	Gauss limited linear	Second order upwind
Diffusion	Gauss linear corrected	Second order
Interpolation	Linear	Linear

3. Results and discussion

In this section, the results for the laminar and turbulent cases are presented, respectively.

3.1. Laminar water hammer

3.1.1. Comparison between different modeling approaches in laminar flow. Figure 5 compares the results of the models used in this study to simulate water hammer. The agreement between the numerical results and the measurements reported by Holmboe and Rouleau [18] is satisfactory. It is evident that the 1D MoC model with the convolution-based unsteady friction formulation is nearly as accurate as the full 3D and 2D axisymmetric CFD simulations. An initial numerical spike at the beginning of the pressure history obtained with the 3D CFD model is observed, which could be attributed to the unrealistic assump-

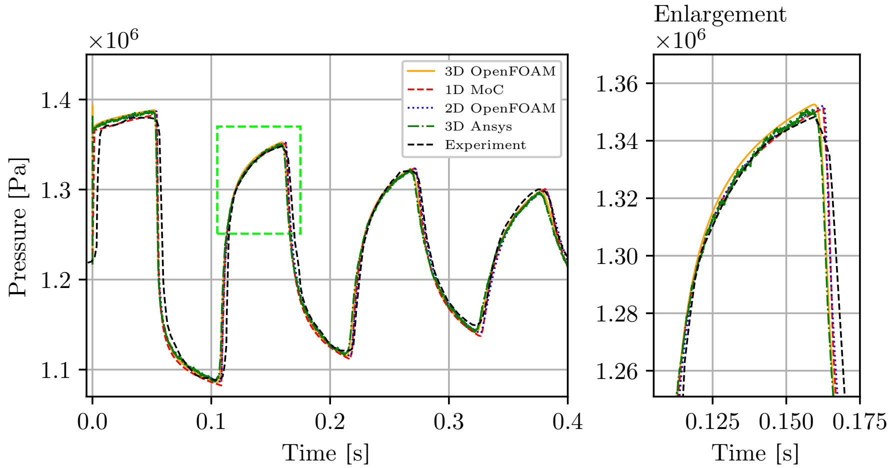

Fig. 5. Pressure attenuation at valve section for laminar test case for different computational models.

tion of abrupt closure of the valve, or insufficient resolution of the computational mesh near the valve boundary. Error values are presented in Table 5.

Table 5. Error value for different models with $\Delta t = 1 \times 10^{-5}$ s.

Model	MAPE [%]
OpenFOAM 3D	1.0050
ANSYS 3D	0.9876
OpenFOAM 2D	0.7527
1D MoC	0.8418

3.1.2. Influence of mesh refinement on solution accuracy in laminar flow. The next step of this study involves a detailed mesh examination for the 3D simulation by running cases with the mesh combinations listed in Table 2. The corresponding pressure histories are shown in Fig. 6. Overall, variations in the axial and circumferential mesh sizes have only a minor effect on the predicted pressure response. It is observed that coarsening the mesh in the axial direction introduces perturbations at the beginning of the pressure signal at the valve section. In addition, as shown in Fig. 6c the radial mesh resolution significantly influences accuracy. Since unsteady friction in the 3D CFD model is captured through near-wall velocity gradients and shear stresses resolved by the computational cells, an insufficient number of cells in the radial direction can lead to an inaccurate prediction of wave attenuation. The squared shape of the pressure wave indicates incorrect numerical diffusion and insufficient resolution for the wall shear-stress calculation. The results for relatively high λ_r are very close to

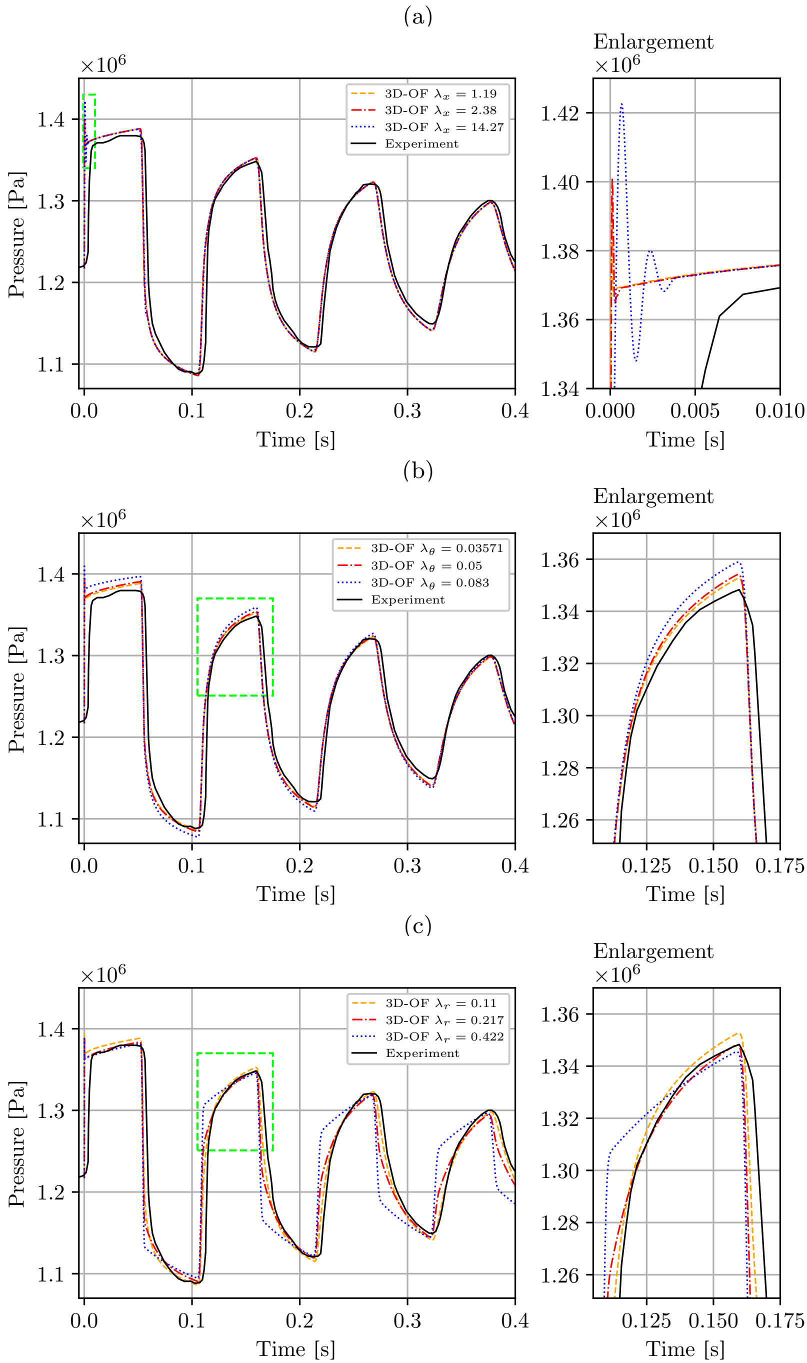

Fig. 6. Pressure attenuation at valve section for laminar test case for different mesh resolutions in (a) axial, (b) circumferential and (c) radial directions.

TABLE 6. Error value for different mesh sizes in laminar case via OpenFOAM with $\Delta t = 1 \times 10^{-5}$ s.

<table>
<tr><th>λ_x</th><th>λ_θ</th><th>λ_r</th><th>N_{cells}</th><th>MAPE [%]</th></tr>
<tr><td>1.19</td><td rowspan="3">0.03571</td><td rowspan="3">0.11</td><td>504,000</td><td>1.005</td></tr>
<tr><td>2.38</td><td>252,000</td><td>1.001</td></tr>
<tr><td>14.27</td><td>42,000</td><td>0.986</td></tr>
<tr><td rowspan="2">1.19</td><td>0.05</td><td rowspan="2">0.11</td><td>222,000</td><td>1.066</td></tr>
<tr><td>0.083</td><td>126,000</td><td>1.30</td></tr>
<tr><td rowspan="2">1.19</td><td rowspan="2">0.03571</td><td>0.217</td><td>312,000</td><td>1.329</td></tr>
<tr><td>0.422</td><td>264,000</td><td>2.38</td></tr>
</table>

quasi-steady 1D model results. To present the results of the mesh study, error value for the investigated mesh sizes is summarized in Table 6.

3.1.3. Influence of time-step size on solution accuracy in laminar flow. In the next stage, the effect of time-step size on the 3D CFD results is examined. The Courant number (Co) is defined as:

$$\text{Co} = \frac{(c + v_{max})\Delta t}{\Delta x}, \tag{3.1}$$

where Δt is the time-step size and Δx is the size of one computational cell in the axial direction. v_{max} is the maximal modulus of the axial velocity component while the maximum is taken over the whole domain. This dimensionless number helps to investigate the influence of time-step size on solution accuracy. Figure 7 compares pressure histories obtained with different Courant numbers.

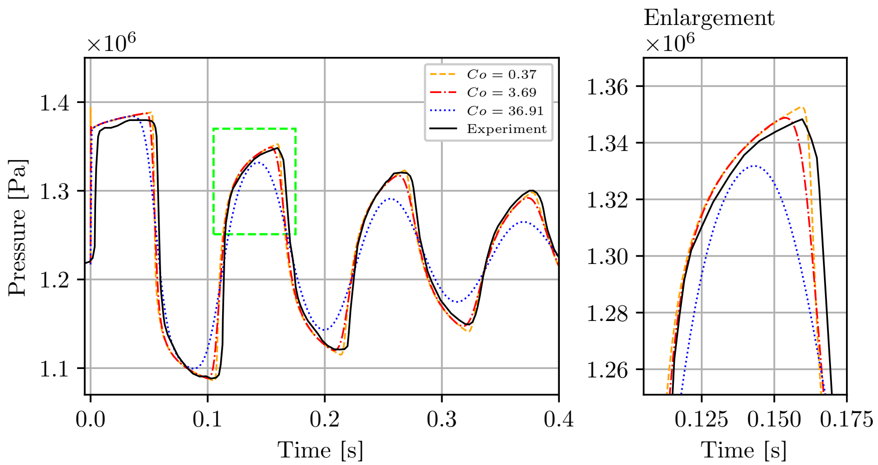

FIG. 7. Pressure attenuation at valve section for laminar test case for different time-steps.

It is evident from table 7 that a Courant–Friedrichs–Lewy condition Co < 1 is suitable for the present study. Larger Co leads to over-damped pressure waves, as the temporal discretization becomes insufficient to capture sharp pressure variations propagating at the acoustic wave speed in the liquid.

Error value for different time-step sizes is summarized in Table 7. It is evident that MAPE increases as larger time-steps are chosen for the simulation. Larger Co is clearly leading to inaccurate results and artificial damping of the pressure wave which has been quantified by MAPE.

TABLE 7. Error value for different time-steps via OpenFOAM.

Δt [s]	MAPE [%]	Courant number
1×10^{-5}	1.005	0.37
1×10^{-4}	1.011	3.69
1×10^{-3}	1.867	36.91

3.1.4. Velocity profile and wall shear stress in laminar flow. Figure 8(a) shows that the velocity at $t = 0$ s has the parabolic shape expected for fully developed laminar velocity profile. From one extremum to the next, the velocity profile in the core region of the pipe has flattened, while its magnitude decreases due to viscous dissipation.

Figure 8(b) presents the corresponding profiles at local minima of the mean velocity, where the flow has reversed direction. Although the velocity is negative over almost the entire cross-section, the profile in the core region remains relatively smooth. In contrast, a steep velocity gradient develops near the pipe

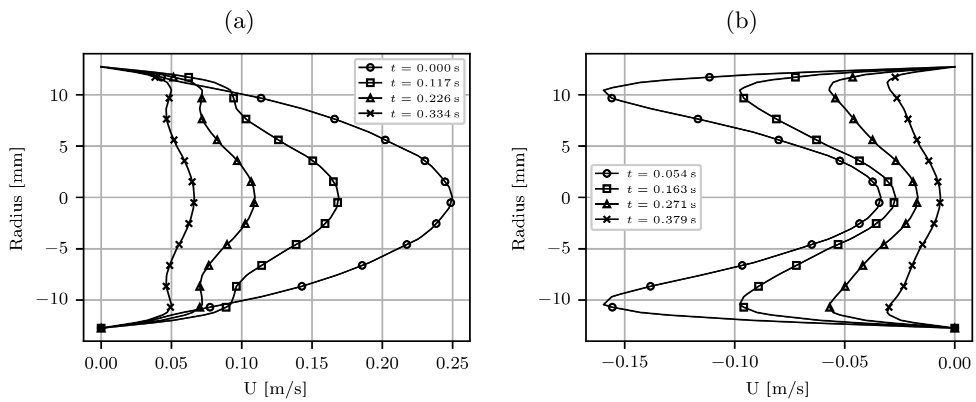

FIG. 8. Laminar velocity profiles at the pipe middle section for successive local (a) maximum and (b) minimum values of the cross-sectional mean velocity.

wall. This indicates that the core region (approximately 80% of the pipe radius) is dominated by inertia effects, whereas viscous effects are mostly visible near the pipe wall (approximately 20% of the pipe radius).

Figure 9 shows the velocity profiles corresponding to successive instants at which the cross-sectional mean velocity at the pipe middle section is zero. Here, the positive and negative velocity regions coexist within the same cross-section

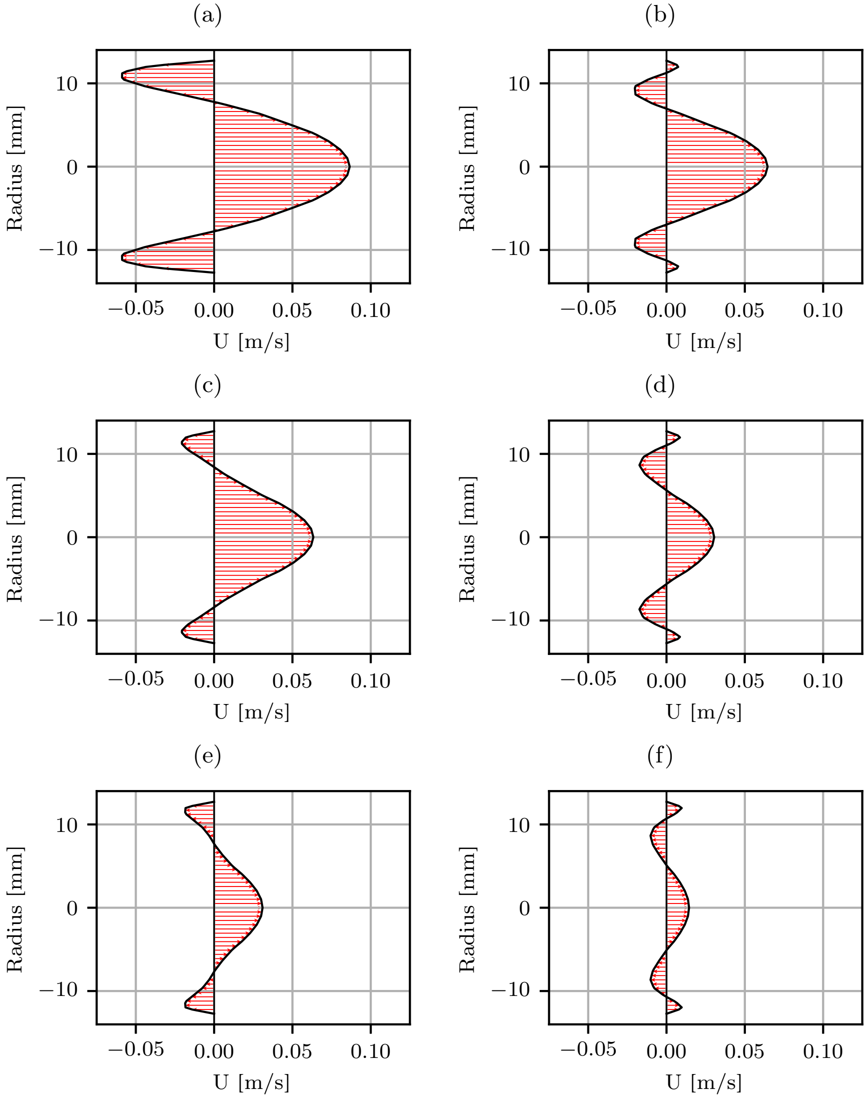

Fig. 9. Laminar velocity profile at the middle section of the pipe in times (a) $t = 0.040$ s, (b) $t = 0.094$ s, (c) $t = 0.148$ s, (d) $t = 0.203$ s, (e) $t = 0.258$ s, (f) $t = 0.314$ s, where the mean cross-sectional velocity is zero.

and cancel each other in the cross-sectional average. However, these profiles show that the flow is not stagnant when the bulk velocity becomes zero.

This observation is important for the modeling of unsteady friction. In a quasi-steady 1D model, the friction term is evaluated from the instantaneous cross-sectional mean velocity. Therefore, when the mean velocity is zero, the quasi-steady friction contribution would also vanish. However, the steep velocity gradients observed in Fig. 9, especially near the pipe wall, indicate that wall shear stress can still be significant. This highlights the limitation of quasi-steady friction model and emphasizes the importance of unsteady friction modeling in 1D water hammer simulations.

At these instants, the coexistence of forward and reverse flow regions is clearly visible. This can be interpreted as a result of the rapid response of the core flow to the pressure wave, where inertia effect is dominant. In contrast, the near-wall region responds more slowly because of viscous effects and the no-slip condition. As a result, the velocity profile passes through a counter-flow state before the whole cross-section adjusts to the new flow direction. The velocity profiles of fully positive and fully negative flows are shown in Figs. 8(a) and 8(b), respectively.

Figure 10 represents the wall shear stress in the middle section of the pipe throughout the whole simulation. It is observed that the convolution-based unsteady friction for the 1D model has yielded results close to the full 3D. This suggests that the convolution-based unsteady friction formulation represents the cross-sectional effects of the transient velocity distribution well. It is also evident that at instants when the mean velocity is zero (such as $t = 0.040$ s and $t = 0.094$ s), the wall shear stress modeled by 1D method is not zero. This means that this model is capable of taking the velocity profile variation in a single cross-section into account.

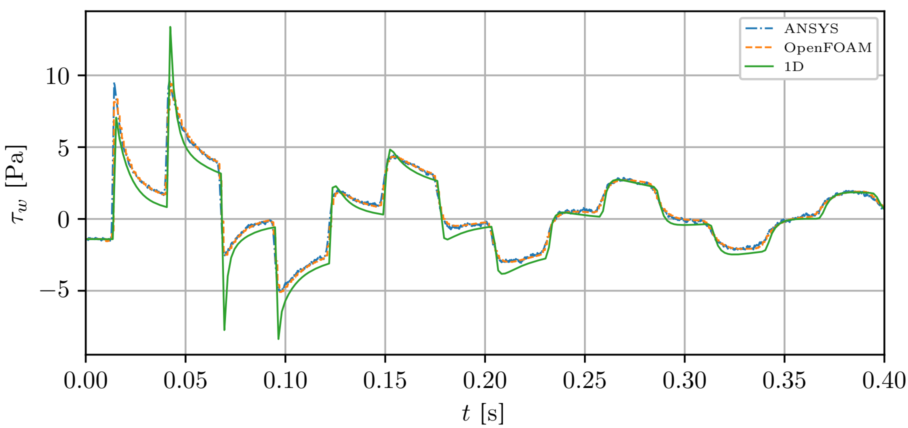

Fig. 10. Wall shear stress in the middle section of the pipe in laminar flow.

3.2. Turbulent water hammer

3.2.1. Comparison between different modeling approaches in turbulent flow. Figure 11 shows the comparison between different computational models and the experimental measurements. A qualitatively satisfactory agreement is achieved between the simulations and the experiment. However, the 3D ANSYS results provide a more accurate qualitative and quantitative representation of wave attenuation compared to the other models. Error values are summarized in Table 8 for different numerical models. The higher MAPE value in the turbulent case, compared with the laminar case, is likely related to the strong oscillations in wave amplitude and the associated uncertainty in the experimental measurements.

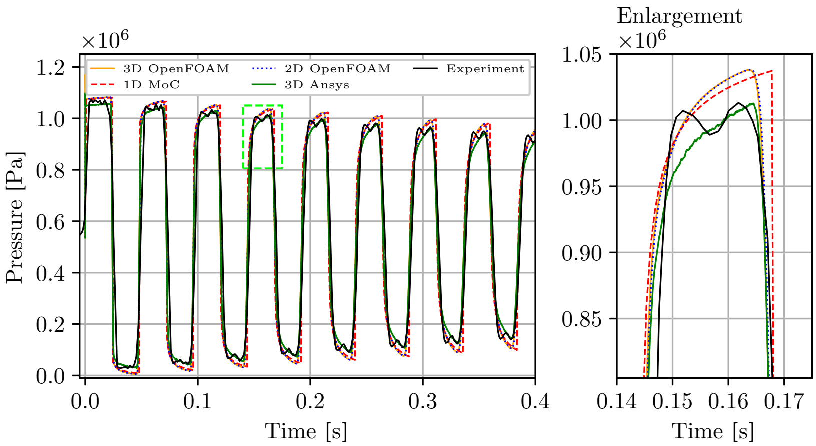

FIG. 11. Pressure attenuation at valve section for turbulent test case for different computational models.

TABLE 8. Error value for different turbulent models with $\Delta t = 1 \times 10^{-5}$ s.

Model	MAPE [%]
OpenFOAM 3D	21.273
ANSYS 3D	15.350
OpenFOAM 2D	20.452
1D MoC	22.587

3.2.2. Influence of mesh refinement on solution accuracy in turbulent flow. A mesh study is also carried out for the turbulent case using the metrics listed in Table 2. The results are presented in Fig. 12 for mesh refinement in each direction. Similar to the laminar case, refining the mesh in the axial and circumferential directions yields nearly identical pressure histories. Therefore, the

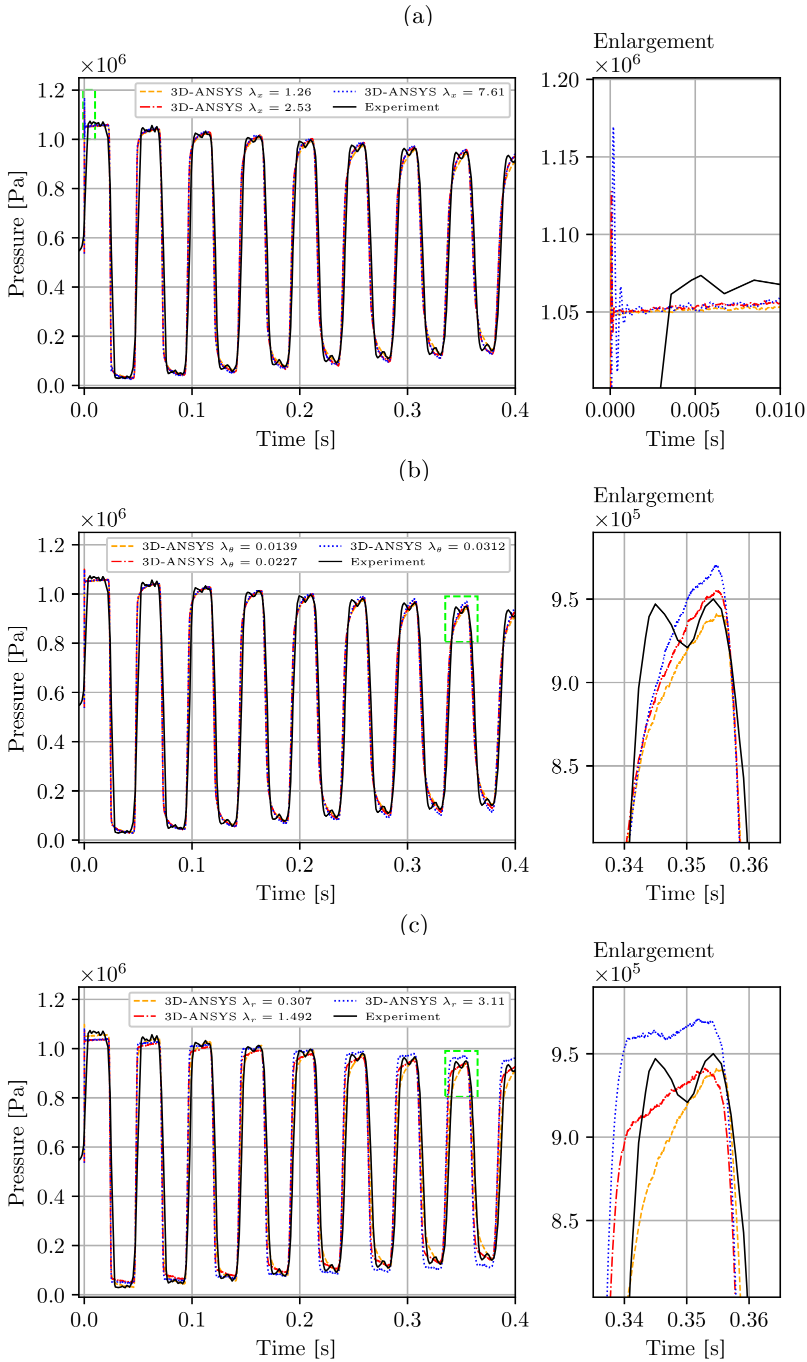

FIG. 12. Pressure attenuation at valve section for turbulent test case for different mesh resolutions in (a) axial, (b) circumferential, and (c) radial directions.

pressure response at the valve section is not heavily sensitive to mesh size in these directions. In contrast, the mesh resolution in the radial direction affects the predicted pressure waves, since the wall shear stress depends on the near-wall velocity gradient and insufficient radial resolution can reduce accuracy. As it is evident in Fig. 12c, pressure results for $\lambda_r = 3.11$ are close to quasi-steady friction modeling, meaning that unsteady friction is not modeled correctly. The results obtained for increased λ_r not only exhibit incorrect wave dissipation, but also show numerical dispersion and inaccurate wave timing. The values for MAPE are indicated in Table 9.

TABLE 9. Error value for different mesh sizes of turbulent case via ANSYS with $\Delta t = 1 \times 10^{-5}$ s.

<table>
<tr><th>λ_x</th><th>λ_θ</th><th>λ_r</th><th>N_{cells}</th><th>MAPE [%]</th></tr>
<tr><td>1.26</td><td rowspan="3">0.0139</td><td rowspan="3">0.307</td><td>1,285,000</td><td>15.350</td></tr>
<tr><td>2.53</td><td>642,500</td><td>15.137</td></tr>
<tr><td>7.61</td><td>215,000</td><td>15.452</td></tr>
<tr><td rowspan="2">1.26</td><td>0.0227</td><td rowspan="2">0.307</td><td>754,500</td><td>15.623</td></tr>
<tr><td>0.0312</td><td>532,000</td><td>16.029</td></tr>
<tr><td rowspan="2">1.26</td><td rowspan="2">0.0139</td><td>1.492</td><td>964,000</td><td>22.047</td></tr>
<tr><td>3.11</td><td>680,500</td><td>23.293</td></tr>
</table>

3.2.3. Influence of time-step size on solution accuracy in turbulent flow. In the next stage, the effect of time-step is examined. As shown in Fig. 13, the simulation results deviate from the experimental measurements as the Courant number increases. This deviation is attributed to insufficient temporal resolution to capture the steep pressure variations propagating at the acoustic wave speed in

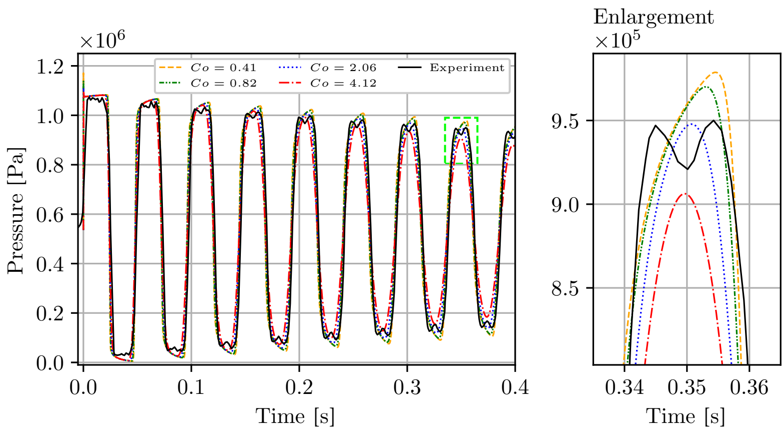

FIG. 13. Pressure attenuation at valve section for turbulent test case for different time-steps via OpenFOAM.

the liquid domain. For the time-step study, the most accurate pressure histories (capturing both the peak amplitude and wave timing) are obtained with $Co = 0.41$ and $Co = 0.82$. As with the laminar test case, here the wave CFL condition is $Co < 1$. The error values for different time-steps are presented in Table 10. It is evident that larger time-step results in overdamped amplitude in the solution.

TABLE 10. Error value for different time-steps of turbulent case via OpenFOAM.

Δt [s]	MAPE [%]	Courant number
1×10^{-5}	21.273	0.41
2×10^{-5}	19.824	0.82
5×10^{-5}	21.411	2.06
1×10^{-4}	29.521	4.12

3.2.4. Velocity profile and wall shear stress in turbulent flow. Figures 14(a) and 14(b) illustrate the velocity profiles of local maxima and minima of the mean cross-sectional velocity in the middle section of the pipe. Compared to the laminar test case shown in Fig. 8, the velocity profile is not represented by a parabolic shape and it is flatter in the core region. This indicates that inertia is more dominant in the core region of the pipe, whereas the viscous sublayer is thinner compared to the laminar test case. Comparing the profiles of local maxima and minima, it can be observed that the shape of the profile in the core region remained more or less the same, while steep gradients are evident near the wall (approximately 5 % of the pipe diameter).

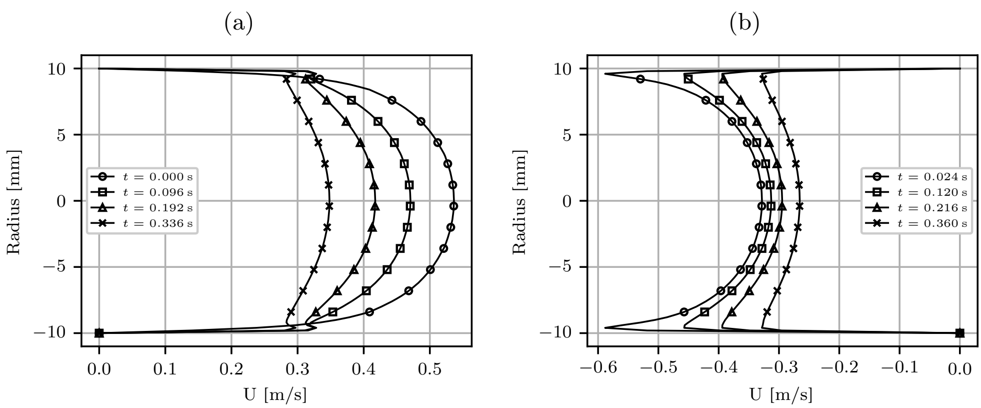

FIG. 14. Turbulent velocity profiles at the pipe middle section for successive local (a) maximum and (b) minimum values of the cross-sectional mean velocity.

Figure 15 represents the velocity profile at instants when the cross-sectional mean velocity in the middle section of the pipe reaches zero. A strong counter-flow is observed at these instants which is the reason why the mean velocity is zero. In fact, from observing these profiles, it is understood that the fluid is not stationary and rather still in motion from the 2D point of view. Therefore, although the mean velocity is zero, the unsteady friction is still affecting the flow and cannot be assumed to be insignificant.

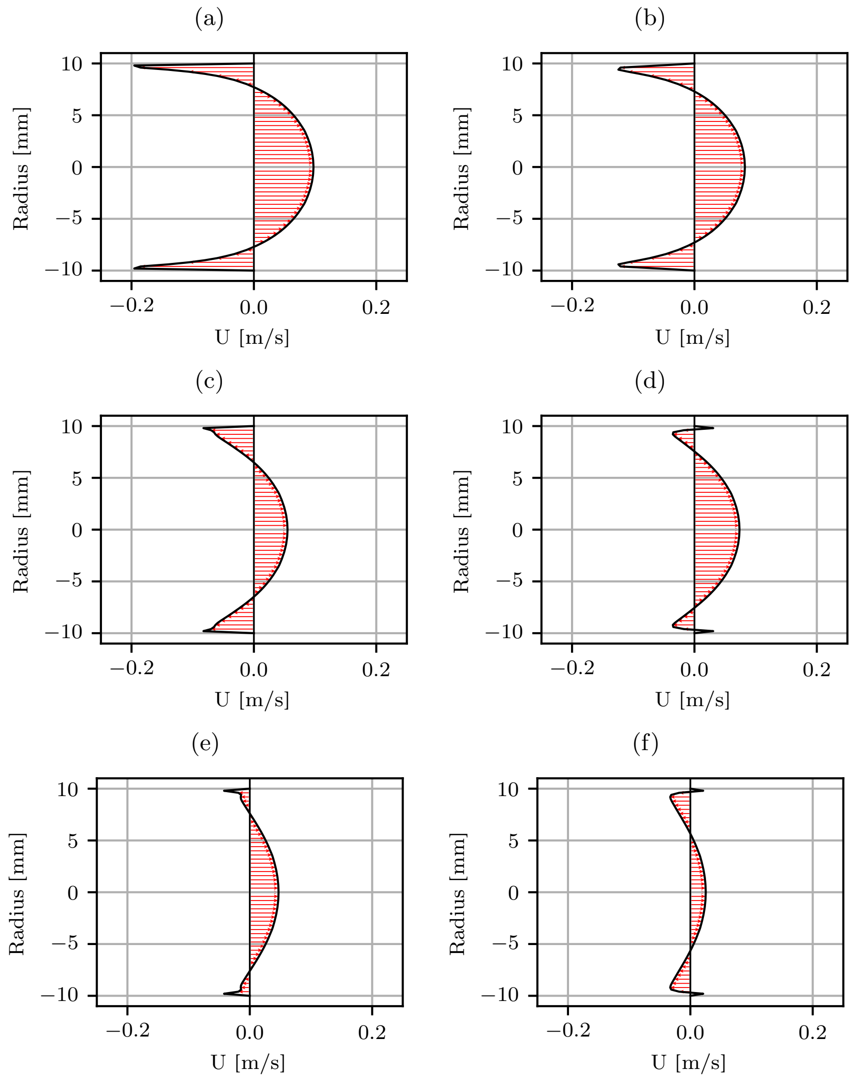

Fig. 15. Turbulent velocity profile at the middle section of the pipe in times (a) $t = 0.017$ s, (b) $t = 0.040$ s, (c) $t = 0.160$ s, (d) $t = 0.183$ s, (e) $t = 0.351$ s, (f) $t = 0.375$ s, where the mean cross-sectional velocity is zero.

This phenomenon happens because the core region of the pipe reacts almost instantly to the pressure wave passing the middle section of the pipe, before this effect reaches the near-wall region where viscous effects are dominant. These instants are basically the moment between local maxima and minima of the mean velocity, represented in Figs. 14(a) and 14(b), respectively.

Figure 16 illustrates the wall shear stress in the middle section of the pipe in the turbulent test case. This shows that the 1D wall shear stress modeling has yielded results close to 3D modeling. At some instants where the mean cross-sectional velocity is zero (such as $t = 0.017$ s and $t = 0.16$ s) wall shear stress is still significant and correctly predicted by the convolution-based integration method within the 1D framework.

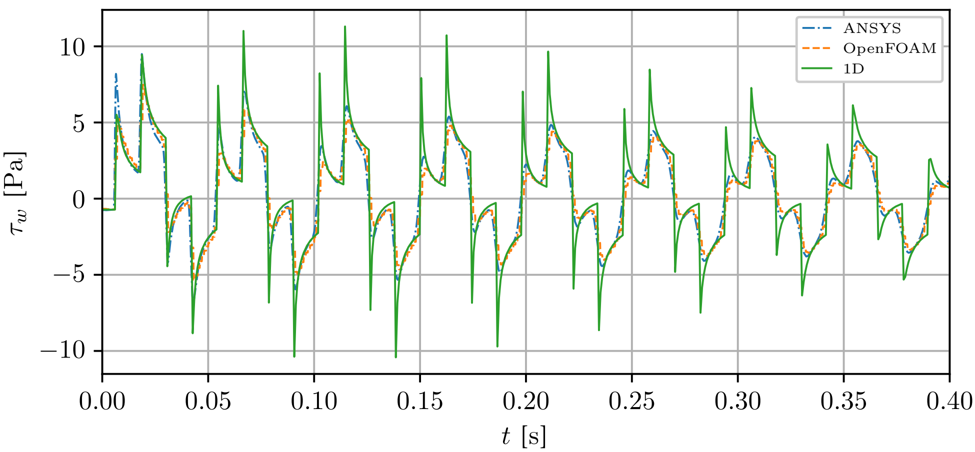

Fig. 16. Wall shear stress in the middle section of the pipe in turbulent flow.

3.2.5. k–ϵ **turbulence model.** Due to the highly dissipative nature of the k–ϵ model, wall functions are typically employed for high-Reynolds-number flows [35]. Since the standard k–ϵ model relies on log-law wall functions, the first computational cell must be located within the logarithmic region of the boundary layer. Accordingly, it is recommended to select the first-layer thickness such that the dimensionless wall distance satisfies $30 \leq y^+ \leq 500$ [36]. For the present test case, this corresponds to a first-layer thickness of approximately 1 mm. While this choice provides accurate velocity and pressure predictions under steady-state conditions, it fails to correctly capture the transient behavior associated with water hammer. Figure 17 presents the pressure response predicted by this model, which shows nearly identical results to the 1D quasi-steady model.

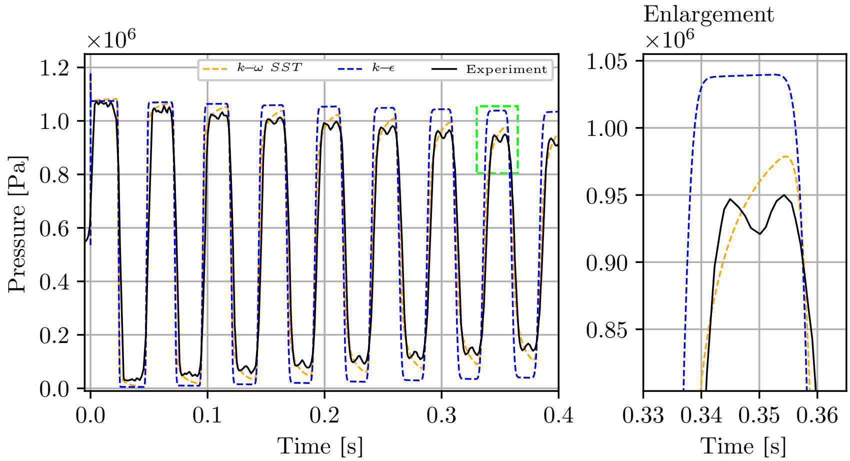

FIG. 17. Pressure attenuation at valve section for turbulent test case using k–ω SST and k–ϵ model via OpenFOAM.

4. Conclusions

This study focused on 1D MoC, 2D axisymmetric, and full 3D CFD simulations of valve-induced water hammer in a reservoir–pipe–valve (RPV) system for both laminar and turbulent test cases. In both regimes, the numerical results showed reasonable agreement with experimental measurements. The turbulent simulations exhibited higher deviations in terms of mean absolute percentage error; however, they still demonstrated qualitatively good agreement with the experimental data.

In both cases, the 3D simulation results did not provide significantly more accurate predictions compared to the 2D axisymmetric model. This indicates that the analyzed system behaves predominantly two-dimensionally. Since no 3D physics were explicitly introduced to the solution domain, the velocity profile remained symmetric and no significant circumferential gradient was observed. Although the 3D model seems unnecessary and generates redundant data at the expense of more computational time, the 3D mesh analysis provides further insight into this subject area and serves as a foundation for more complicated problems with more complex physics involved. Moreover, comparing 2D and 3D to 1D MoC in terms of pressure attenuation at the valve section did not indicate meaningful improvement in accuracy. This means that pressure attenuation at the valve section can be accurately computed in the current RPV case using the one-dimensional model. The primary distinction between the higher-dimensional Finite Volume Method and 1D MoC is the treatment of unsteady friction. In the 1D model, unsteady friction must be introduced explicitly, whereas in the

2D and 3D CFD simulations it is captured intrinsically using the gradient of velocity within the finite volume framework. This aspect becomes particularly relevant in asymmetric flows, where unsteady friction modeling may be more complex.

The 3D mesh analysis showed that variations in axial and circumferential mesh resolution had negligible influence on the accuracy of the results. In contrast, radial mesh refinement significantly affected the predicted pressure response, as it directly governs the near-wall velocity gradient and shear stress calculation. This confirms that water hammer in the considered RPV system is essentially axisymmetric, with dominant gradients in the axial (pressure and velocity) and radial (velocity) directions. In addition, the time-step sensitivity analysis indicated that sufficiently small time-steps are required to accurately capture transient pressure wave propagation without introducing additional numerical damping.

From the comparison of the two turbulence models, k–ω SST and k–ϵ, it was observed that the latter is not suitable for the present test case, primarily due to the relatively low Reynolds number and its reliance on high-Re wall functions. Although maintaining $30 \leq y^+ \leq 500$ yields correct steady-state results, the transient simulations produce pressure attenuation behavior similar to the quasi-steady model.

This study provides a foundation for the development of extended water hammer models incorporating additional physical phenomena such as cavitation and fluid–structure interaction. Furthermore, it demonstrates the potential for coupling 1D and 3D models to combine the computational efficiency of 1D approaches with the spatial resolution capabilities of 3D CFD.

Acknowledgements

This research was supported by funding from the Science Development Fund of Faculty of Mechanical Engineering and Mechatronics under project No. 856-007000-07002. Kamil Urbanowicz declares that his contribution is financially supported by the Minister of Science under the 'Regional Initiative of Excellence' (RID) programme.

References

1. M.S. Ghidaoui, M. Zhao, D.A. McInnis, D.H. Axworthy, *A review of water hammer theory and practice*, ASME. Applied Mechanics Review, **58**, 1, 49–76, 2005, https://doi.org/10.1115/1.1828050.

2. M.S. Ghidaoui, *On the fundamental equations of water hammer*, Urban Water Journal, **1**, 2, 70–83, 2004, https://doi.org/10.1080/15730620412331290001.

3. K. Urbanowicz, A. Bergant, M. Stosiak, A. Deptula, M. Karpenko, M. Kubrak, A. Kodura, *Water hammer simulation using simplified convolution-based unsteady friction model*, Water, **14**, 19, 3135, 2022, https://doi.org/10.3390/w14193151.

4. A.E. Vardy, J.M. Brown, *Evaluation of unsteady wall shear stress by Zielke's method*, Journal of Hydraulic Engineering, **136**, 7, 453–456, 2010, https://doi.org/10.1061/(ASCE)HY.1943-7900.0000192.

5. M. Lewandowski, A. Adamkowski, *Experimental verification of 1D-simulation method of water hammer induced in two series-connected pipes of different diameters: Determination of the Pressure Wave Speed*, Applied Sciences, **14**, 16, 7173, 2024, https://doi.org/10.3390/app14167173.

6. K. Urbanowicz, D.M. Andrade, M. Kubrak, A. Kodura, *Accuracy and limitations of 1D and Q2D water hammer models for laminar and turbulent flows*, Journal of the Brazilian Society of Mechanical Sciences and Engineering, **47**, 12, 666, 2025, https://doi.org/10.1007/s40430-025-05924-z.

7. N.M.C. Martins, D.I. Covas, C. Capponi, S. Meniconi, B. Brunone, *Unified approach for damping rate of transient laminar flow: Experiments, computational fluid dynamics, and one-dimensional, and global models*, Journal of Fluids Engineering, **146**, 2, 021306, 2024, https://doi.org/10.1115/1.4063697.

8. S. Henclik, *Investigations of column separation influence on pressure waves severity based on results of water hammer experiments in elastically supported pipeline*, Archives of Mechanics, **77**, 6, 621–645, 2025, https://doi.org/10.24423/aom.4741.

9. N.M.C. Martins, N.J. Carrico, H.M. Ramos, D.I. Covas, *Velocity-distribution in pressurized pipe flow using CFD: Accuracy and mesh analysis*, Computers and Fluids, **105**, 218–230, 2014, https://doi.org/10.1016/j.compfluid.2014.09.031.

10. S. Saemi, M. Raisee, M.J. Cervantes, A. Nourbakhsh, *Computation of two-and three-dimensional water hammer flows*, Journal of Hydraulic Research, **57**, 3, 386–404, 2019, https://doi.org/10.1080/00221686.2018.1459892.

11. N.M.C. Martins, E.M. Wahba, *On the hierarchy of models for pipe transients: from quasi-2d water hammer models to full 3D CFD models*, Journal of Pressure Vessel Technology, **144**, 2, 021402, 2022, https://doi.org/10.1115/1.4051930.

12. Y. Cao, L. Zhou, C. Ou, H. Fang, D. Liu, *3D CFD simulation and analysis of transient flow in a water pipeline*, AQUA–Water Infrastructure, Ecosystems and Society, **71**, 6, 751–767, 2022, https://doi.org/10.2166/aqua.2022.023.

13. M.K. Neyestanaki, G. Dunca, P. Jonsson, M.J. Cervantes, *A Comparison of different methods for modelling water hammer valve closure with CFD*, Water, **15**, 8, 1510, 2023, https://doi.org/10.3390/w15081510.

14. A. Bergant, Z. Rek, K. Urbanowicz, *Analytical, numerical 1D and 3D water hammer investigations in a simple pipeline apparatus*, Strojniški vestnik-Journal of Mechanical Engineering, **71**, 5–6, 149–156, 2025, https://doi.org/10.5545/sv-jme.2024.1179.

15. N.M.C. Martins, D.I. Covas, B. Brunone, S. Meniconi, C. Capponi, *CFD-based transient analysis for the detection and characterisation of extended partial blockages in pipes*, Fluids, **10**, 11, 291, 2025, https://doi.org/10.3390/fluids10110291.

16. N. Vovk, J. Ravnik, *Comparison of 1D Euler equation based and 3D Navier–Stokes simulation methods for water hammer phenomena*, Strojniški vestnik-Journal of Mechanical Engineering, **71**, 9–10, 337–348, 2025, https://doi.org/10.5545/sv-jme.2025.1340.

17. V. Maskani, M. Nabipour, E. Behnamtalab, *Numerical simulation of water hammer phenomenon using ANSYS Fluent: A comparative analysis with analytical models and laboratory data*, Applied Water Science, **15**, 293, 2025, https://doi.org/10.1007/s13201-025-02643-7.

18. E.L. Holmboe, W.T. Rouleau, *The effect of viscous shear on transients in liquid lines*, Journal of Fluids Engineering, **89**, 1, 174–180, 1967, https://doi.org/10.1115/1.3609549.

19. A.K. Soares, N.M.C. Martins, D.I. Covas, *Transient vaporous cavitation in a horizontal copper pipe*, Journal of Hydraulic Research, **55**, 5, 731–736, 2017, https://doi.org/10.1080/00221686.2017.1286394.

20. M.H. Chaudhry, *Applied Hydraulic Transients* 3rd ed., Springer, 2014, https://doi.org/10.1007/978-1-4614-8538-4.

21. E.B. Wylie, V.L. Streeter, L. Suo, *Fluid Transients in Systems*, Prentice-Hall Inc., Englewood Cliffs, 1993.

22. W. Zielke, *Frequency-dependent friction in transient pipe flow*, Journal of Basic Engineering, **90**, 1, 109–115, 1968, https://doi.org/10.1115/1.3605049.

23. K. Urbanowicz, *Computational compliance criteria in water hammer modelling*, E3S Web of Conferences, **19**, 03021, 2017, https://doi.org/10.1051/e3sconf/20171903021.

24. V.M. Canuto, *Compressible turbulence*, The Astrophysical Journal, **482**, 2, 827, 1997, https://doi.org/10.1086/304175.

25. D.C. Wilcox, *Turbulence modeling for CFD*, 3rd ed., La Cañada: DCW Industries Inc, 2006, https://doi.org/10.1017/S0022112095211388.

26. R. Manceau, *Turbulence modeling for CFD*, Master. Pau, France, 2023, https://inria.hal.science/hal-03207433v6.

27. F.R. Menter, *Two-equation eddy-viscosity turbulence models for engineering applications*, AIAA Journal, **32**, 8, 1598–1605, 1994, https://doi.org/10.2514/3.12149.

28. Q. Sun, X. Wang, Y. Wu, Y. Xu, Z. Wang, *Sensitivity of creep parameters to pressure fluctuation of transient flow in viscoelastic pipes*, Journal of Hydroinformatics, **26**, 7, 1753–1770, 2024, https://doi.org/10.2166/hydro.2024.116.

29. Q. Sun, Z. Zhang, Y. Wu, H. Liang, *Numerical analysis of transient pressure damping in viscoelastic pipes at different water temperatures*, Materials, **15**, 14, 4904, 2022, https://doi.org/10.3390/ma15144904.

30. Z.G. Tao, L. Zhou, Y. Li, Y. Huang, Y.Q. Lu, Y.Y. Hu, R.L. Feng, *Transient response and analytical solution of burst phenomenon in long distance water pipeline*, Engineering Applications of Computational Fluid Mechanics, **19**, 1, 2451171, 2025, https://doi.org/10.1080/19942060.2025.2451171.

31. J.H. Ferziger, M. Perić, R.L. Street, *Computational Methods for Fluid Dynamics* 4th ed., Springer, 2020, https://doi.org/10.1007/978-3-319-99693-6.

32. *OpenFOAM v13 User Guide*, The OpenFOAM Foundation, https://doc.cfd.direct/openfoam/user-guide/.

33. H. Jasak, *Error Analysis and Estimation for the Finite Volume Method with Applications to Fluid Flows*, Imperial College, University of London, 1996.

34. P.K. Sweby, *High resolution schemes using flux limiters for hyperbolic conservation laws*, SIAM Journal on Numerical Analysis, **21**, 5, 995–1011, 1984, https://doi.org/10.1137/0721062.

35. B.E. Launder, D.B. Spalding, *The numerical computation of turbulent flows*, Computer Methods in Applied Mechanics and Engineering, **3**, 2, 269–289, 1974, https://doi.org/10.1016/0045-7825(74)90029-2.

36. H.K. Versteeg, *An Introduction to Computational Fluid Dynamics the Finite Volume Method*, 2nd ed., Pearson Education India, 2007.

Received March 16, 2026; revised version July 28, 2026.
Published online August 14, 2026.